Naval Research Laboratory

Washington, DC 20375-5320

NRL/MR/6382--97-7901

A Preliminary Investigation of the Microstructure and Mechanical Properties of Porous Polymers

R.K. Everett
D.P. Harvey, II
P. Matic
R.S. Schechter
N.K. Batra
K.E. Simmonds

Mechanics of Materials Branch
Materials Science and Technology Division

A. Kee

Geo-Centers, Inc.
Fort Washington, MD

February 28, 1997

DISCLAIMER NOTICE

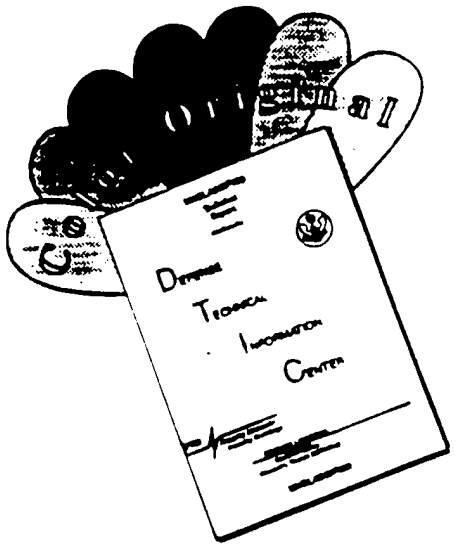

THIS DOCUMENT IS BEST QUALITY AVAILABLE. THE COPY FURNISHED TO DTIC CONTAINED A SIGNIFICANT NUMBER OF COLOR PAGES WHICH DO NOT REPRODUCE LEGIBLY ON BLACK AND WHITE MICROFICHE.

REPORT DOCUMENTATION PAGE

Form Approved
OMB No. 0704-0188

1. AGENCY USE ONLY (*Leave Blank*)	2. REPORT DATE	3. REPORT TYPE AND DATES COVERED
	February 28, 1997	

4. TITLE AND SUBTITLE

A Preliminary Investigation of the Microstructure and Mechanical Properties of Porous Polymers

5. FUNDING NUMBERS

6. AUTHOR(S)

R.K. Everett, D.P. Harvey, II, P. Matic, R.S. Schechter, N.K. Batra
K.E. Simmonds and A. Kee*

7. PERFORMING ORGANIZATION NAME(S) AND ADDRESS(ES)

Naval Research Laboratory
Washington, DC 20375-5320

8. PERFORMING ORGANIZATION REPORT NUMBER

NRL/NR/6382--97-7901

9. SPONSORING/MONITORING AGENCY NAME(S) AND ADDRESS(ES)

Office of Naval Research
Arlington, VA 22217

10. SPONSORING/MONITORING AGENCY REPORT NUMBER

11. SUPPLEMENTARY NOTES

*Geo-Centers, Inc.
Fort Washington, MD

12a. DISTRIBUTION/AVAILABILITY STATEMENT

Approved for public release; distribution unlimited.

12b. DISTRIBUTION CODE

13. ABSTRACT (*Maximum 200 words*)

Porous polymers exhibit complex microstructures which affect their mechanical and physical properties. Pores in the microstructure are the result of the addition of Expancel™ polymer microspheres, and potentially by gas entrained during mixing operations. The entrained gas pores can form long strings and sheets which may act as defects in the structure. A combination of direct observation and finite element modeling has shown that accounting for the stiffening effect of the microspheres is important, and that strain localization occurs due to microstructural heterogeneity and interactions generated by the large gas pores. Permanent creep deformations can be imparted to the material in relatively short times, perhaps due to the localizations previously noted. Initial investigations into wave propagation and nondestructive evaluation by microwave dielectrometry were successful.

14. SUBJECT TERMS

Polymer, Microsphere, Foam, Finite element modeling, NDE, Ultrasonic wave propagation, Microwave dielectrometry

15. NUMBER OF PAGES

38

16. PRICE CODE

17. SECURITY CLASSIFICATION OF REPORT	18. SECURITY CLASSIFICATION OF THIS PAGE	19. SECURITY CLASSIFICATION OF ABSTRACT	20. LIMITATION OF ABSTRACT
UNCLASSIFIED	UNCLASSIFIED	UNCLASSIFIED	UL

NSN 7540-01-280-5500

Standard Form 298 (Rev. 2-89)
Prescribed by ANSI Std 239-18
298-102

CONTENTS

A PRELIMINARY INVESTIGATION OF THE MICROSTRUCTURE AND MECHANICAL PROPERTIES OF POROUS POLYMERS

1.0 Introduction

Porous polymers, elastomeric materials containing gas-filled inclusions or pores, represent a class of composite materials with unique, tailorable properties. This type of material may be fabricated by the addition of either a second phase with a lower density or by the addition of a foaming agent prior to curing. The volume fraction of the porosity and the size distribution of the pores may be adapted to suit the application. Uniform porosity or porosity gradients are conceivable.

Porous polymers exhibit several advantageous properties over the "neat" or non-porous versions of the matrix. They can be significantly less dense and more flexible than the neat polymer. Therefore, they have many applications including packaging, cushioning, shock absorption, and noise abatement [1-3].

One difficulty with the performance of current porous polymers is a reported tendency to creep in service [4]. The magnitude of the deformation is on the order of a few percent after exposure to approximately 7 MPa (1000 psi) compressive stress.

In order to investigate the sources and mechanisms of this phenomenon, and to better model the time-dependent behavior of porous polymers in general, a collaboration between NRL and NSWC-Carderock was initiated. NSWC provided materials, fabrication and processing expertise, and experimental data. NRL focused on material microstructural characterization, mechanical modeling via finite elements, and an initial evaluation of both wave propagation and nondestructive evaluation (NDE) of the porous materials. The purpose of this report is to document the initial findings of NRL in this investigation.

2.0 Materials

Two materials were characterized in this investigation: the neat polymer material and a porous material with the same polymer as the matrix. The porous polymer in this investigation was created by mixing commercially-available polymer microspheres with one part of the two liquid polymer precursors, then mixing with the remaining precursor, and pouring into a suitable mold for curing. Samples of both materials were provided to NRL by NSWC-Carderock [5]. Characterization included optical microscopy with digital image analysis and compression testing. The results on the neat polymer will be described first, followed by the porous polymer.

2.1 Neat Material

Neat polymer material was provide to NRL in the approximate form of a semi-cylinder of 8.5 cm radius by 10 cm high (3.5 inch by 4 inch). The sample had a batch designation of Z6Q. The material was translucent and could be cut by knife or band-saw.

Manuscript approved October 30, 1996

Samples of the neat polymer were cut from the main body for microstructural observations and mechanical testing. An approximate cutting plan is shown in Figure 1 which is similar to the one for the porous material discussed below. A column of material through the entire thickness of the sample was used for the microstructural observations. The column was sectioned approximately in half, by cutting with a razor blade, and the two resulting surfaces were viewed under a microscope. Another material region was used for mechanical property data. The neat polymer was more difficult to cut than the porous polymer and the prepared surfaces usually had striations in the direction of the motion of the razor.

The neat polymer material contained spherical pores in a range of sizes. Figure 2 presents micrographs of two typical smaller pores. Pore sizes were observed from approximately 25 μm to 200 μm. No size distribution or volume fraction data were collected on the neat polymer material.

2.1.1 Mechanical Property Data

Mechanical property data on the neat polymer sample were collected for input into the FEM material modeling constitutive equations. Two cubic samples, approximately 13 mm on a side, were tested in uniaxial compression. One specimen approximately 24 x 23 x 2.23 mm was tested in compression to simulate plane strain conditions. Figure 3 presents the average stress-strain response of the neat material in uniaxial compression. The replicate measurements were comparable and data were averaged at a given strain. The plane strain response is shown in Figure 4 along with the uniaxial curve for comparison. Note the lower modulus and the knee in the plane strain stress-strain curve.

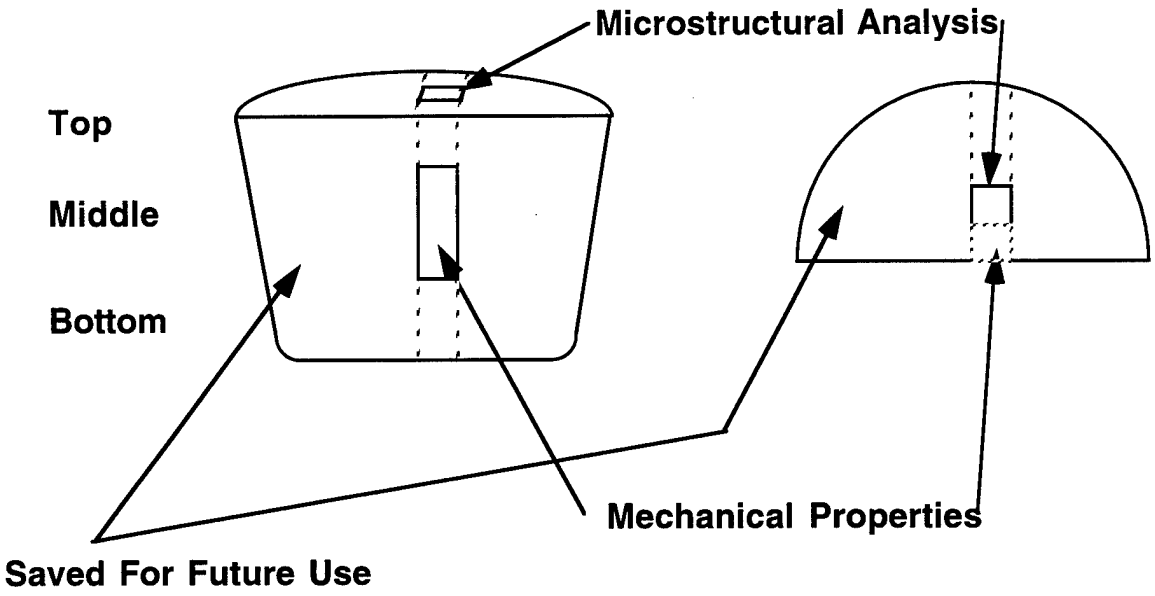

Figure 1 - Cutting plan for the neat polymer sample.

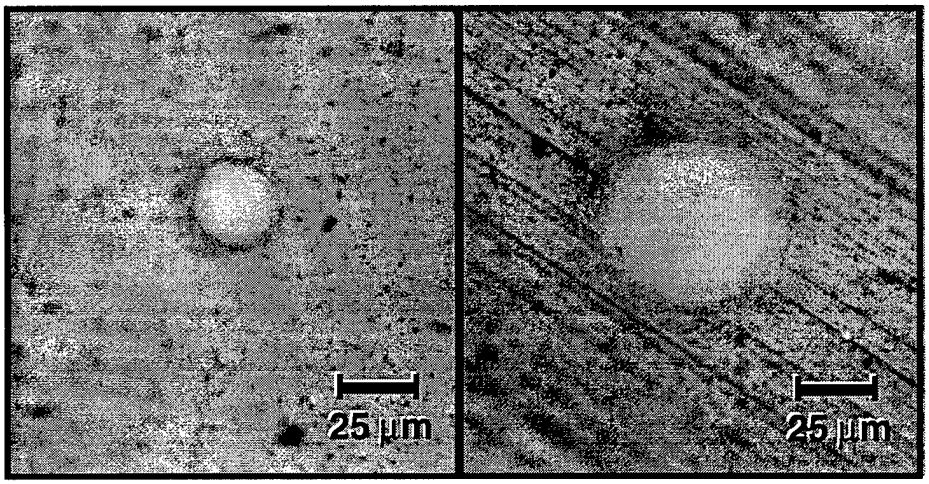

Figure 2 - Micrographs of typical pores in the neat polymer sample.

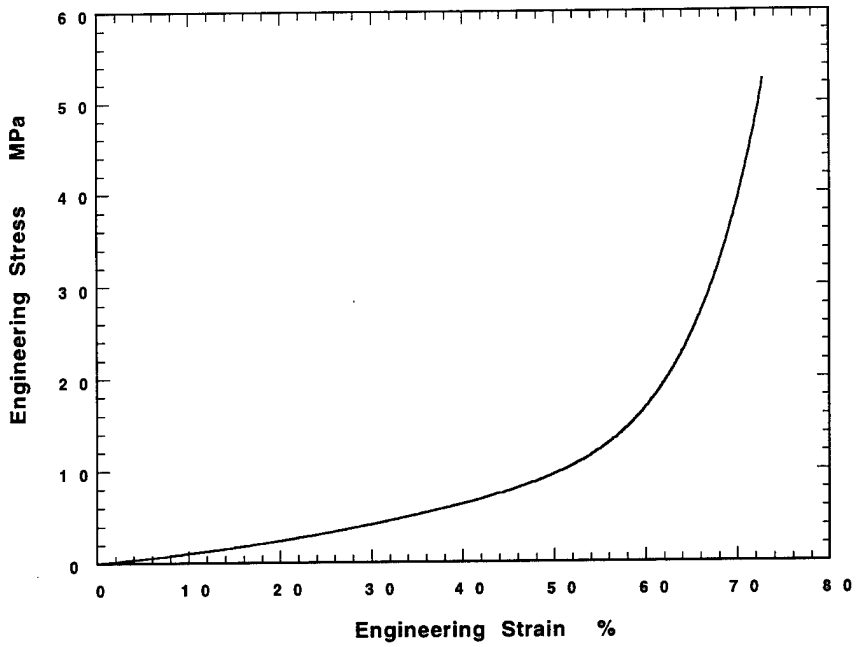

Figure 3 - Uniaxial compression stress-strain curve for the neat polymer sample.

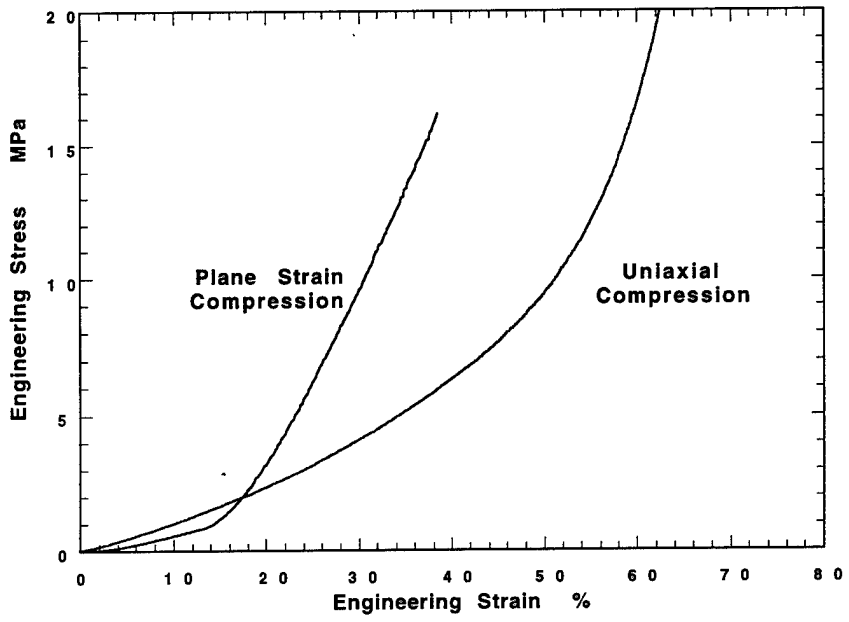

Figure 4 - Plane strain compression stress-strain curve for the neat polymer sample.

2.2 Porous Material

The porous polymer sample provided was half of a 5-quart bucket. The approximate radius was 10 cm by 12 cm high (4 in. by 4.75 in.). The batch designation was #W-96071701-CO2. The material was opaque and white.

2.2.1 Microstructural Studies

Figure 5 presents a cutting diagram for the sample. The microstructural analysis was performed on a 2.54 cm by 2.54 cm column of material the height of the entire sample. Additional samples were cut for use in mechanical testing and NDE. These samples were cut from planes of approximately constant height, in case porosity gradients existed. The column of material used for microstructural analysis was further subdivided into three regions. The top and bottom regions analyzed were located approximately 3 mm away from their respective surfaces. The middle region of the column was also prepared for observation. While both parallel (sectioned at a constant height) and perpendicular orientations were studied, most results presented here were obtained from samples with the parallel orientation. No major differences were noted between the two orientations.

Specimens were prepared for microscopy by several techniques. Surfaces for observation were cut from the column with a single-edged razor blade. The smoothest surfaces were produced by making a single-pass cut (guillotine fashion) through the material. Rocking or "sawing" produced undesirable line artifacts on the surface. Some large defects (2 mm or larger) were visible on the cut surfaces but most samples required further preparations to observe the pores. A mixture of graphite and isopropyl alcohol (Aerodag-G, manufactured by Acheson Colloids Co., Port Huron, MI) was applied to the surface, allowed to sit

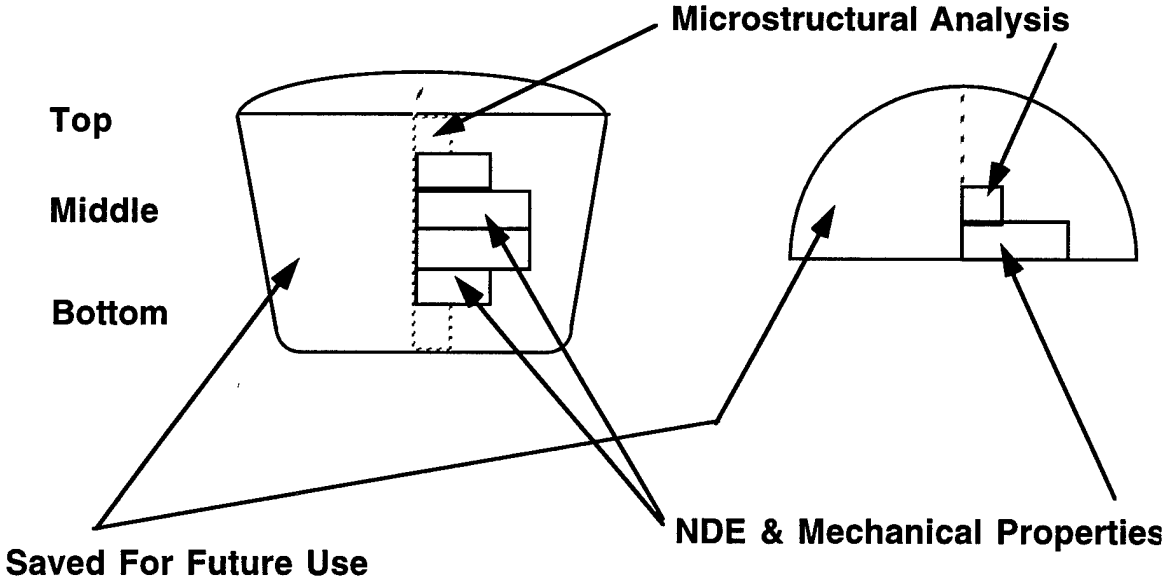

Figure 5 - Cutting plan for the porous polymer sample.

for about 30 seconds, and subsequently wiped off in order to stain the sample. Mercurochrome (antiseptic) also works as a stain.

Samples were viewed in optical light using an inverted-stage Nikon microscope. At low magnifications (50-200X), dark field photography with polarized light gave the best results. At higher magnifications (400-1000X), bright field photography was used to gain sufficient light for an exposure in a reasonable time.

Micrographs of typical regions within the microstructure of the porous polymer are shown in Figure 6. Large variations in pore size are noted. The distribution of the smaller pores appears approximately homogeneous. The larger pores appear to be in localized areas. Further analysis can quantify these trends.

High magnification micrographs reveal that many pores are apparently in very close vicinity or are in contact (Fig. 7). The webs of polymer separating these pores are thin and frequently appear to be buckled. Several causes for the buckling may be envisioned including material fabrication, specimen preparation, and release of internal stresses. In order to eliminate specimen preparation techniques, a separate sample was prepared where the sample cutting direction was tracked and compared to the web bucking directions. No correlation between these directions was observed which leads to the tentative conclusion that some other cause, besides specimen preparation, is responsible.

The pore volume fraction was measured and found to be 0.51. Five 200X magnification micrographs were taken from random positions on samples from each of the top, middle, and bottom regions. The micrographs were digitized at 300 dpi and these files used as input to a digital image analysis program (NIH Image, v. 1.52). The grayscale images were density sliced to select the pores and the area of each feature was measured and stored for comparison to the area of the images. Some editing of the pictures was necessary to correctly discriminate between pores and matrix. Table 1 presents the volume fraction data for the individual regions and the grand average for the pooled data. There is essentially no difference in volume fraction between the regions. Additional measurements, on lower magnification pictures covering larger areas, gave essentially the same results.

The pore size distribution depends upon, but is not uniquely determined by, the microsphere size distribution since entrained gas may also produce pores. The microspheres were identified as the product 091-DE available from Expancel Inc. of Duluth, GA [6]. Product data provided by the manufacturer is given in Table 2.

The pore size distribution was determined experimentally by image analysis in order to verify the manufacturer's data. The feature areas from the top, middle and bottom regions used for the volume fraction analysis were converted to equivalent-area circle diameters. The distribution of the pooled equivalent-circle (Waddel disk) pore diameters is presented in Figure 8. Note the range of sizes is from about 8 to 240 μm, in approximate agreement with the manufacturer's data.

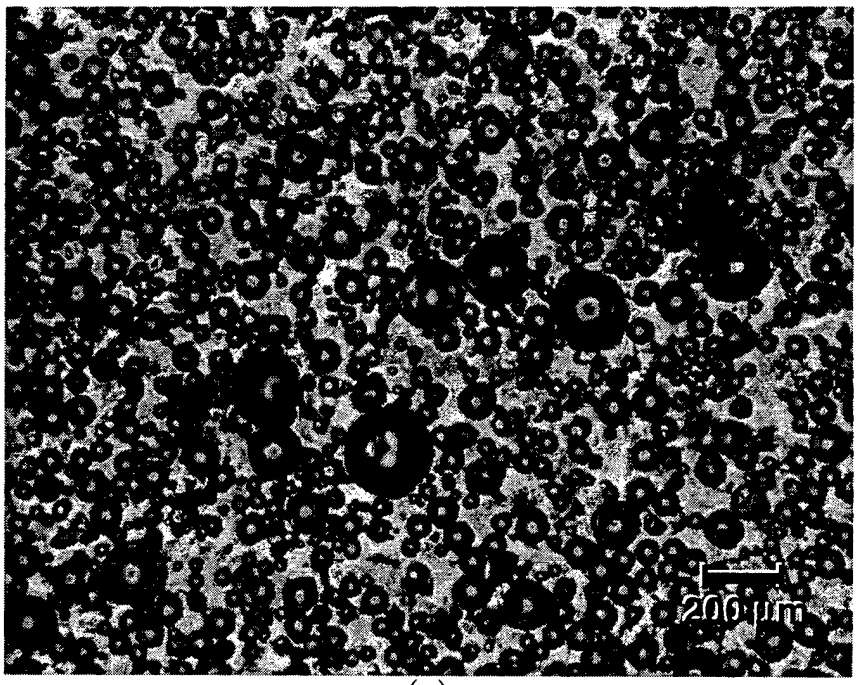

(a)

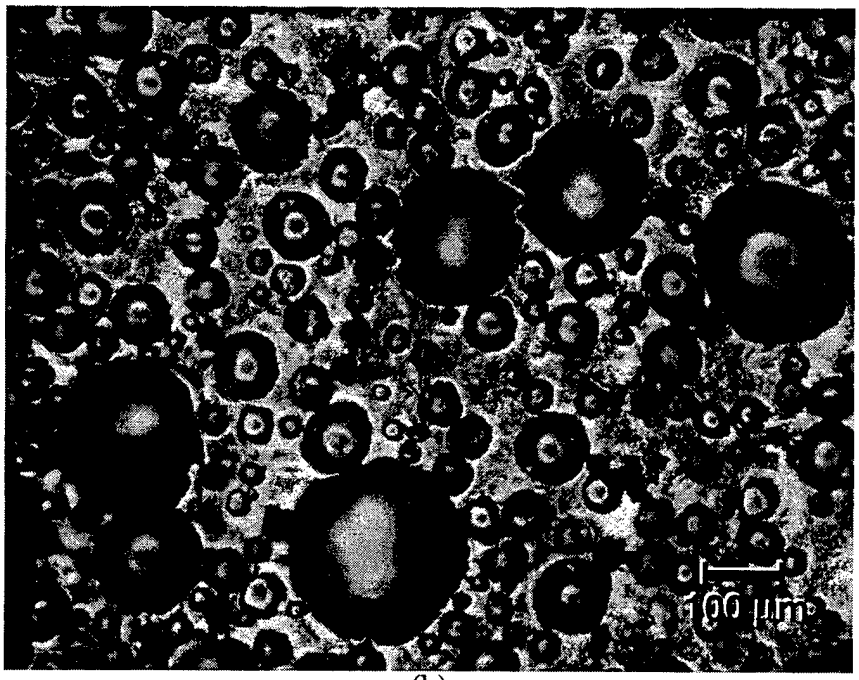

(b)

Figure 6 - Microstructure of porous polymer sample.

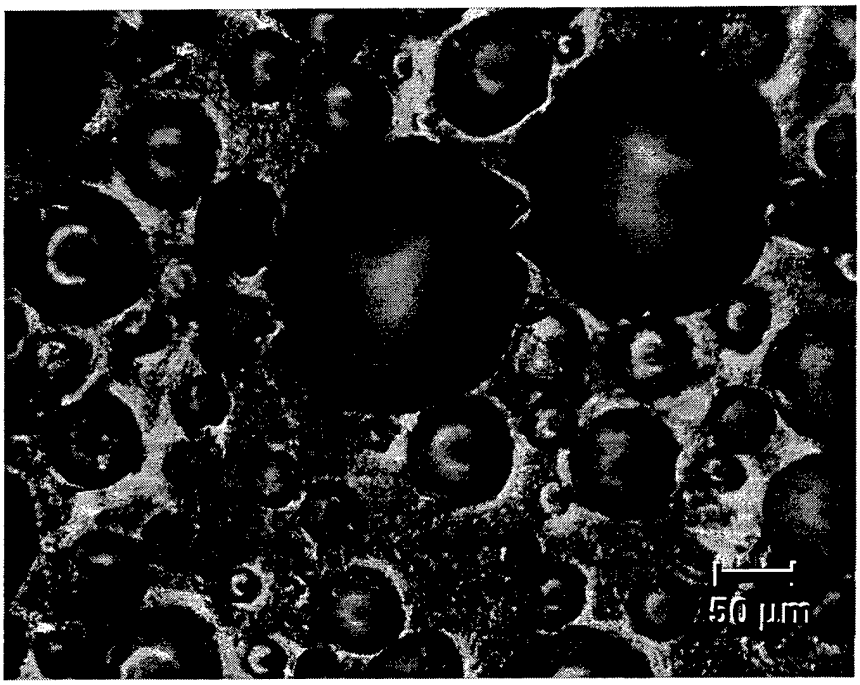

Figure 7 - Polymer webs between pores.

Table 1 - Volume fraction data from porous polymer sample determined by image analysis.

POSITION	MEAN VOLUME FRACTION	STANDARD DEVIATION
Top	0.48	0.04
Middle	0.53	0.03
Bottom	0.51	0.05
Grand Average	0.51	0.04

Table 2 - Manufacturer's product data on Expancel® 091-DE microspheres [6].

Product :	091 DE - "Dry-Expanded"
Sphere Size Range:	10 - 200 μm
Average Diameter (by Weight):	30 -50 μm
Density:	30 kg/m^3
Shell Wall:	≈ 0.1 μm

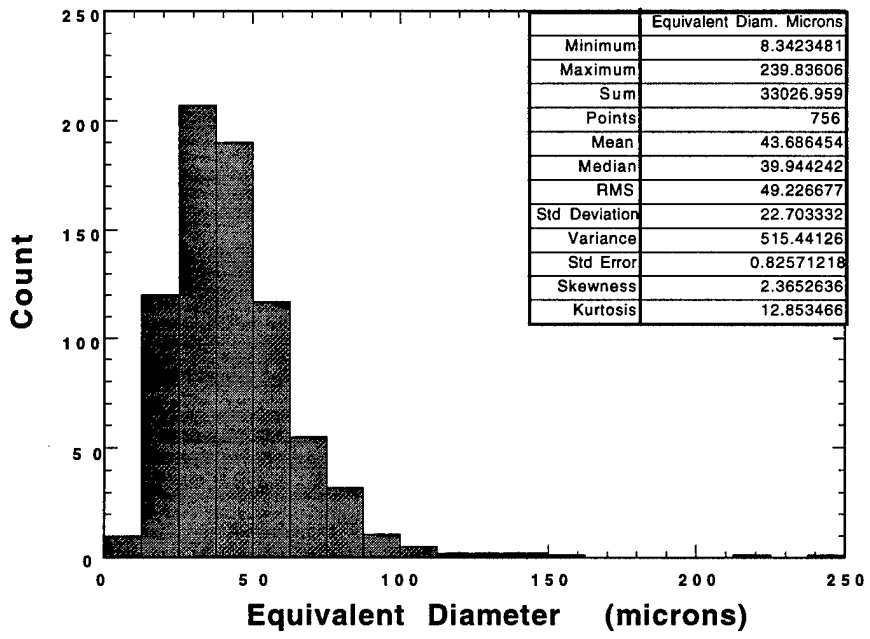

Figure 8 - Equivalent-circle-area feature diameter distribution for data pooled from the top, middle and bottom regions of the porous polymer.

The data from the individual regions indicate some variation in the size distribution through the thickness of the sample studied here. Table 3 shows statistics based on the raw feature data broken down by region.

Table 3 - Feature data, by region, indicating size variation through the thickness of the sample.

Region	Average Diameter (μm)	Standard Deviation	Standard Error
Top	40.95	22.39	1.45
Middle	44.37	24.61	1.51
Bottom	45.55	20.65	1.30

The actual sample population average sphere size and the sphere size distribution must be calculated from the pooled data in Fig. 8 since those data represent measurements on circular sections of spheres. The easiest assumption to make is that the data are from a single size class of uniform-diameter spheres. In that case, the mean of the distribution in Fig. 8 represents two-thirds of the uniform sphere diameter. This procedure yields an average sphere size of 65 μm. However, given the micrographs shown above, this assumption is not warranted and another approach is required.

In a situation where the features of interest are all of similar shape, but are of different sizes, a Saltykov (or Area) analysis may be useful [7]. Briefly, diameter size classes are defined based upon the feature areas. Only the largest diameter spheres in the distribution can contribute to the largest measured diameter class, regardless of where the sphere is cut. The next smaller measured diameter class is populated by both spheres of the next smaller size class and the largest diameter spheres sectioned at an appropriate height to appear as if they were in the smaller size class. Since the probability of cutting a sphere at a height to yield an apparent circle area may be calculated based on its diameter and shape, the contribution that the largest class makes to the next smaller class may be determined. Appropriate modifications to the next smaller diameter class distribution can then be made. The process may be repeated to yield the entire distribution. The results for such an analysis are presented in Figure 9. The number of pores per unit volume (in mm^3) is reported for each diameter size class. Note that the distribution has the approximate shape of a normal curve when plotted against the logarithm of the diameter indicating a log normal distribution of sphere sizes. As a check, an upper bound to the total pore volume fraction may be estimated by summing the product of the pore density of each class and the volume occupied by the maximum sphere size for that class. The

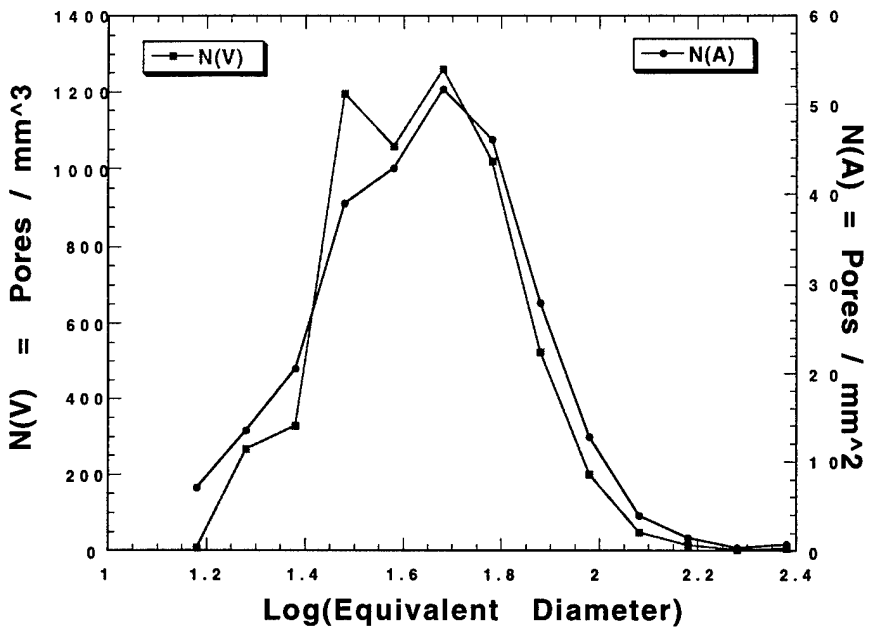

Figure 9 - Pore size distribution derived from equivalent-circle data using a Saltykov analysis.

result is a total volume fraction of approximately 0.55 in good agreement with earlier measurements.

The spatial distribution of the pores was analyzed using several tessellation-based techniques [8]. Dirichlet tessellations were used to define a region-of-influence (a cell) around each pore feature in several micrographs. Statistics on local volume fraction (pore area/cell area), nearest-neighbor distance, and the number of near neighbors were collected. These statistics are compared to the results of random patterns subjected to the same analysis. Two random patterns containing 1000 circles each were generated such that they had the same total volume fraction of circles and that the circles had the same log-normal distribution of sizes as measured in the porous samples.

Table 4 presents the results of this comparison between the random patterns and the porous microstructures. The local volume fraction standard deviations of both the random and porous structures are large due to the log-normal pore distributions. The porous polymer standard deviation is slightly larger than that of the random pattern which usually indicates feature clustering [8]. An additional metric which tracks clustering is the skewness of the nearest-neighbor distance distribution. Note that the skewness of the porous sample is larger than that of the random sample corroborating the clustering. Furthermore, the porous

microstructures have fewer near neighbors than random, and the difference in size between a pore's average nearest-neighbor' diameter is accentuated. These may indicate that there is a preference (i.e., greater than random chance) for the small diameter pores to reside next to large pores in the porous material.

Table 4 - Results of tessellation analysis for spatial distribution.

Metric	Random Pattern	Porous Polymer
Local Volume Fraction Distribution Standard Deviation	0.15617	0.15655
Nearest-Neighbor Distance Distribution Skewness	1.3863	1.7936
Mean Number of Near Neighbors	5.9272	5.8327
Mean Diameter of Nearest-Neighbor	55.62	57.996

In the course of this investigation, several macro-scale microstructural features were noted during sample preparation. Since the effects of these features are, as yet, unknown, documentation was deemed important. Figure 10 presents optical micrographs showing many large pores aligned along curves in the sample. These appear to be swirls of gas bubbles trapped in the polymer, perhaps produced during blending of the precursor-sphere mixture. These void sheets were observed in the parallel orientation (constant height). The average size of the large voids was estimated from measurements made on micrographs. Figure 11 presents the size data and shows an average feature size of approximately 230 μm (no sphere correction applied). Note that the maximum size (544 μm) is over twice as large.

2.2.2 Mechanical Property Data

Mechanical property data on the porous polymer sample were collected for comparison with the FEM modeling experiments. Cubic samples, approximately 13 mm on a side, were tested in uniaxial compression. Multiple specimens (two minimum) from each of two orientations (parallel and perpendicular) were tested. Figure 12 presents the stress-strain response of the porous material in the thickness direction. The reproducibility was good and no orientation dependence was observed.

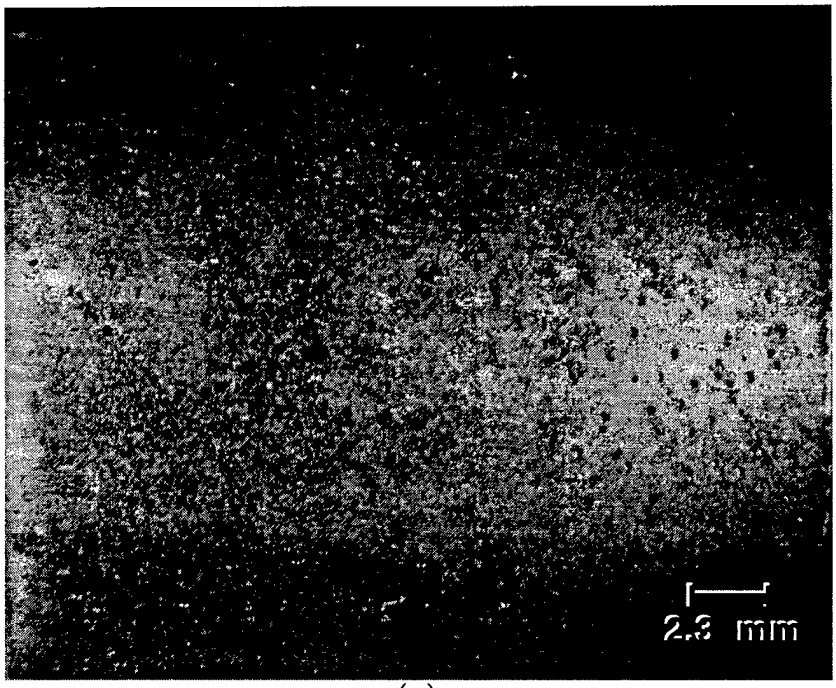

(a)

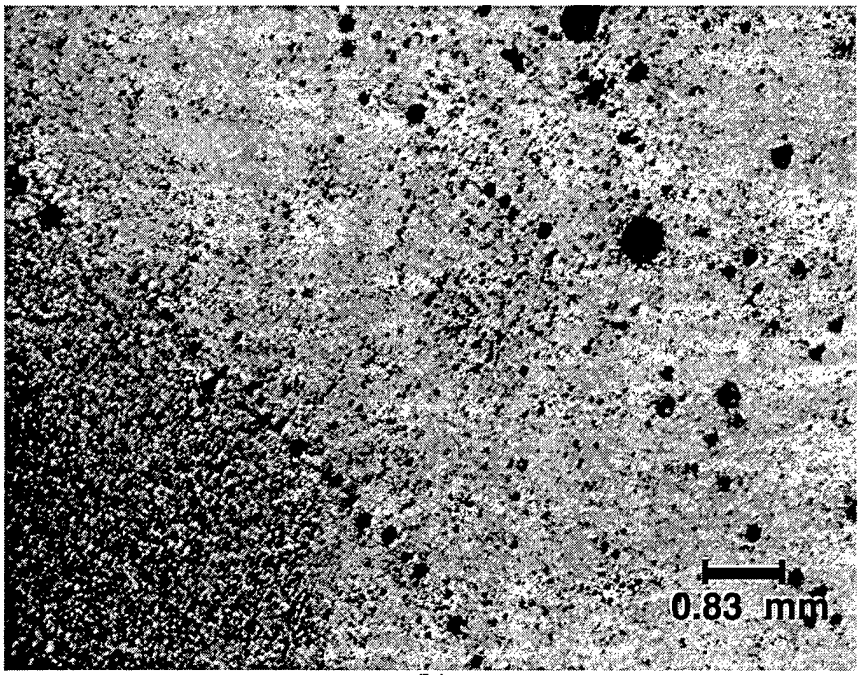

(b)

Figure 10 - Large aligned voids in porous polymer sample.

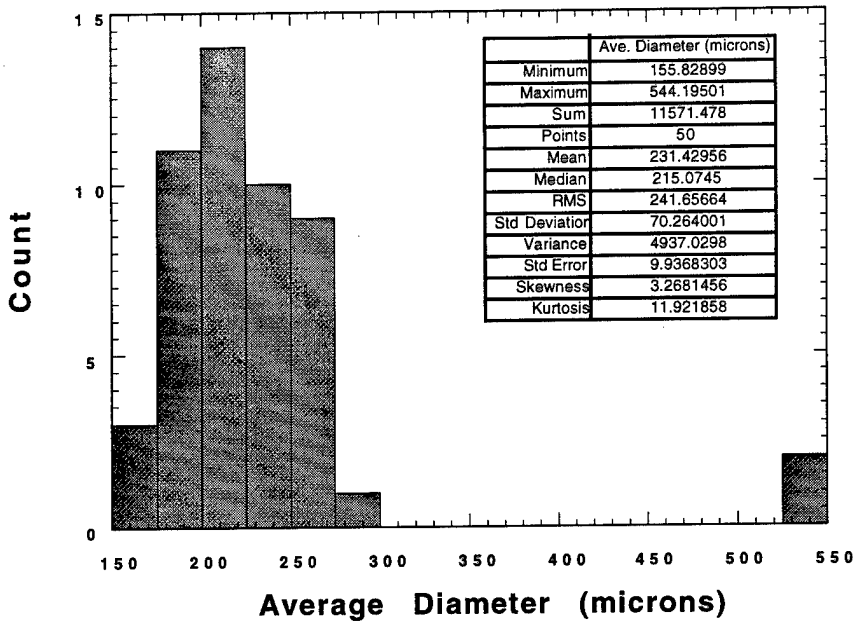

	Ave. Diameter (microns)
Minimum	155.82899
Maximum	544.19501
Sum	11571.478
Points	50
Mean	231.42956
Median	215.0745
RMS	241.65664
Std Deviation	70.264001
Variance	4937.0298
Std Error	9.9368303
Skewness	3.2681456
Kurtosis	11.921858

Figure 11 - Large pore size distribution data.

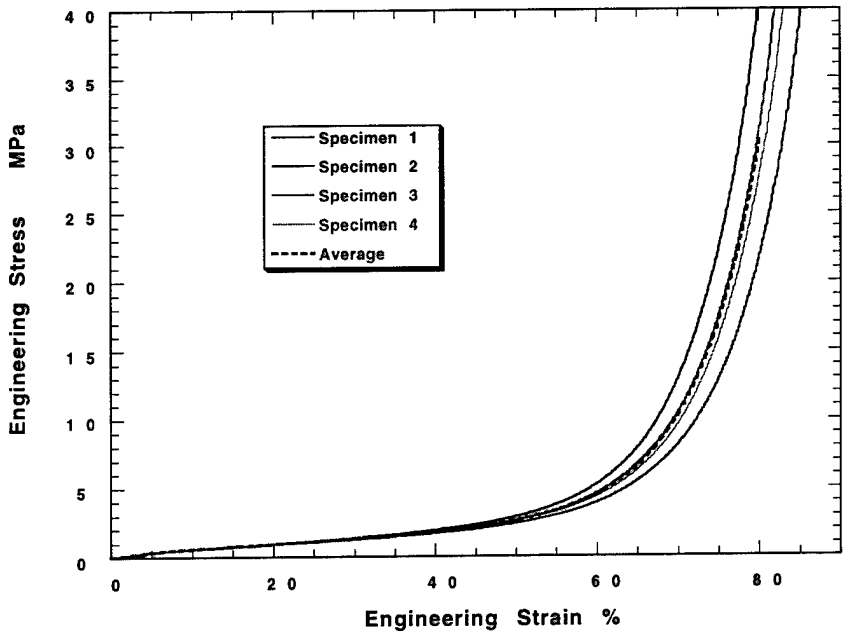

Figure 12 - Porous polymer compression stress-strain curves.

The issue of time-dependent material response was addressed by a series of simple preliminary experiments designed to test whether a permanent deformation could be induced in the porous polymer sample. Three small parallelpipeds of the porous polymer, approximately 2.54 cm x 2.54 cm x 1 cm each, were placed in three different environments and allowed to equilibrate for several hours to the respective ambient temperatures. The environments investigated were: (1) a standard laboratory office, (2) a refrigerator, and (3) a freezer. The temperature of each environment was measured with a standard wall thermometer to be approximately 23.9, 6.1 and -5.5 °C (75, 43, and 22 °F respectively). The samples were then compressed to a strain of 43% using copper disks as platens and c-clamps to apply known, calibrated deormations. The fixtures had also been equilibrated at each temperature before starting. The samples were left overnight in each environment for a total of twelve hours. At the end of that period, the c-clamps were released and the change of thickness versus time was recorded for each sample. The samples were maintained in their respective environments during the experiment, except for short durations when they were removed for measurement.

Figure 13 presents the strain versus time data for the three samples held at three different temperatures. The initial recovery of each sample was temperature dependent with the highest temperature sample recovering most. Quickly (within 20 minutes), the samples returned to within about 3% strain of the initial starting configuration. The refrigerated sample remained at this level during the remaining time under observation, while the other two samples continued to recover an additional small amount. At the end of two hours, the room temperature and the freezer samples exhibited permanent sets on the order of -2% strain. This experiment indicates that the mechanical response of the porous polymer is not extremely temperature sensitive and that apparently permanent deformations may be induced in the laboratory in some accelerated manner. This should greatly facilitate experiments into the underlying phenomena causing the deformation.

2.2.3 Deformation Study

Deformation studies were conducted as a means of determining which microstructural features were interacting under load to produce high local matrix material strains at the material mesoscale (pore-neighborhood and pore-pore interactions). A method was devised to hold a prepared porous sample in a c-clamp under a uniaxial compressive load. The applied strains are estimated to be approximately 15%. The clamped sample was placed on the stage of a microscope and photographed. Various regions of the sample could be viewed under both "no load" and "compressed" conditions to see how the microstructured responded.

Figure 14 presents a pair of micrographs from a relatively uniform region of the porous sample. While there is a range of sphere sizes present in the unloaded case (a), it is comparatively small and no single sphere dominates the microstructure. Under load (b) the composite deforms approximately uniformly with the spheres in no single region being grossly distorted.

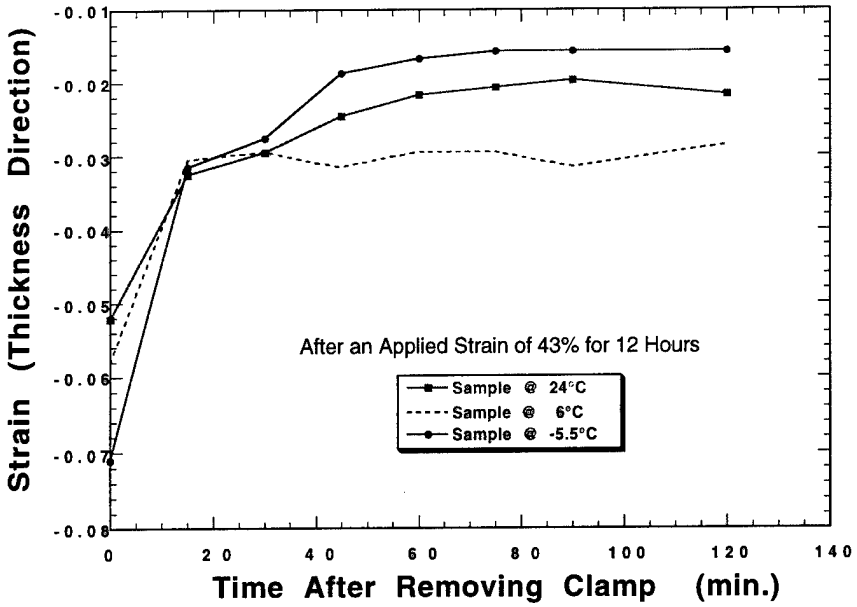

Figure 13 - Pseudo-creep experiment for porous polymer.

In contrast, the behavior exhibited by a non-uniform region of the composite microstructure is very heterogeneous. Figure 15 displays a pair of micrographs from a region containing two large dominant pores. These features are believed to be of the large pore variety, attributed to gas entrainment noted above, and may not be an Expancel® microsphere. Note that under load the large pores undergo large deformations accounting for the majority of the strain in that local region. Furthermore, note the localization of the deformations of the smaller pores in the area between the large pores. These micrographs suggest that the large pores may be deleterious and a source of localization causing large strain concentrations which may, in turn, promote the observed detrimental time-dependent behavior.

As a first order approximation, the degree of non-homogeneous deformation that a local region undergoes may be highlighted by difference images. A difference image can be created by subtracting the grayscale value of a pixel from one image from the grayscale value of a similarly positioned pixel in another image. In the present case the two images involved can be the "compressed" image and a scaled "no load" image. The scaled "no load" image is formed by selecting an area of the "no load" image which contains all of the features (microspheres) found in the final "compressed" image. Typically, this area will be taller and thinner than the "compressed" image. The selected area is then scaled (by pixel arithmetic) to the size of the "compressed" image which is

conceptually similar to applying a homogeneous compression in one direction and a stretching in the other. If a compressed image represented a perfectly homogeneous deformation of the "no load" image with no local variations (concentrations) and no pore rotations, the difference image would appear a uniform gray color. Variations between images appear as dark or light "ghost images" depending on which initial image they came from.

Figure 16 presents the difference images from the uniform region (see Fig. 14) and the non-uniform region (see Fig. 15). The difference image from the uniform region (Fig. 16a) appears to give a good match, especially along the image top left-to-bottom right diagonal. Features along this diagonal have almost disappeared into a uniform gray. Features on either side of this line appear to have a similar shape, but also seem to have been rotated slightly either up or down with respect to the "compressed" image. The scaled image of the uniform region appears to capture much of the behavior of the "compressed" region.

The difference image from the non-uniform region, Figure 16b, shows little agreement between the scaled and "compressed" images. The discrepancies between the scaled and the "compressed" large pores are quite noticeable. The smaller features are similarly inconsistent. These indicate that localized deformation field exist in the "compressed" image.

The work reported above demonstrates the effects of the mesoscale microstructural interactions on the mechanical response of the porous polymer material.

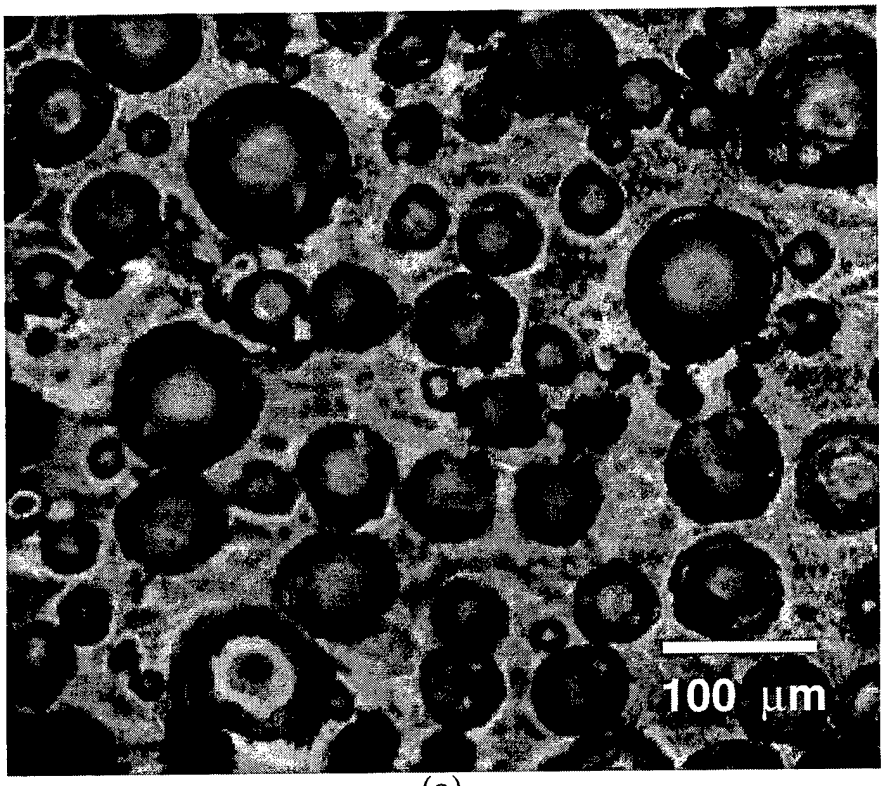

(a)

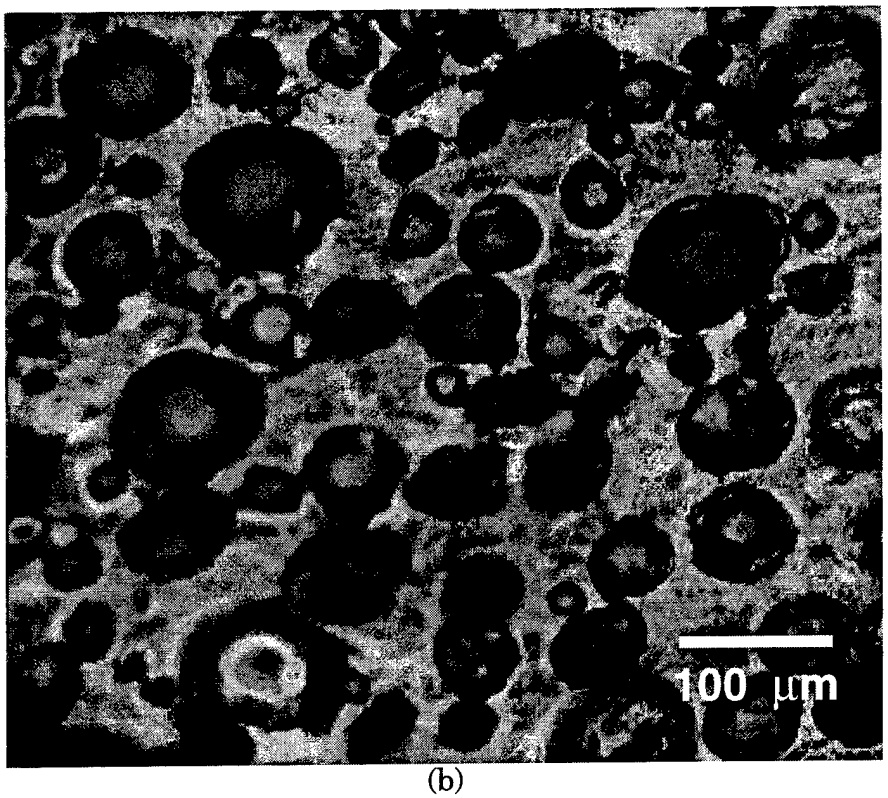

(b)

Figure 14 - Micrographs of porous polymer region with uniform microstructure in the unloaded (a), and compressed (b), states.

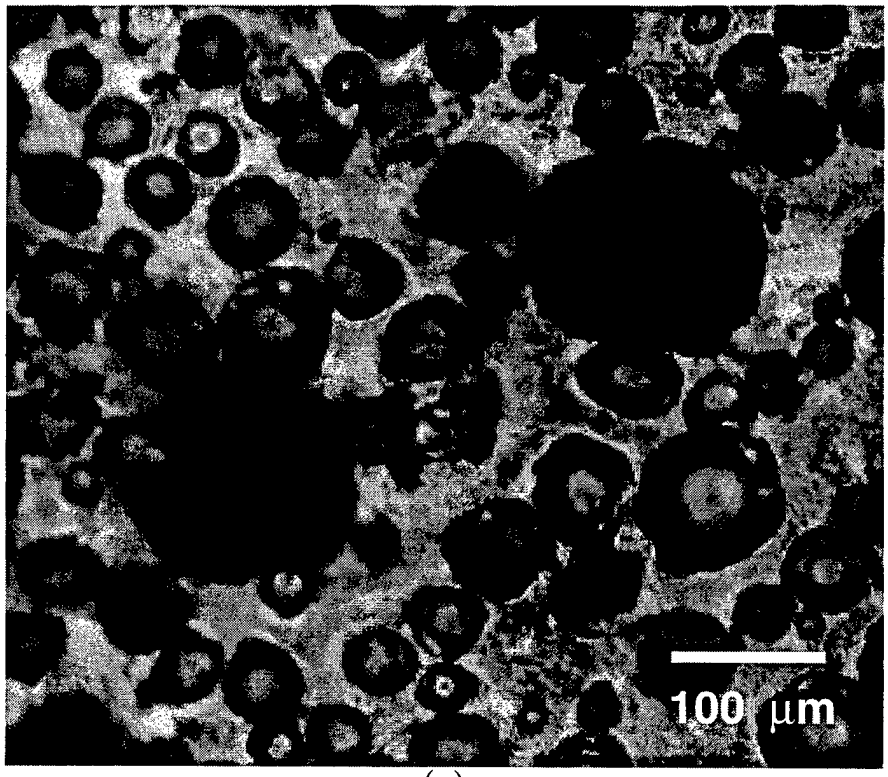

(a)

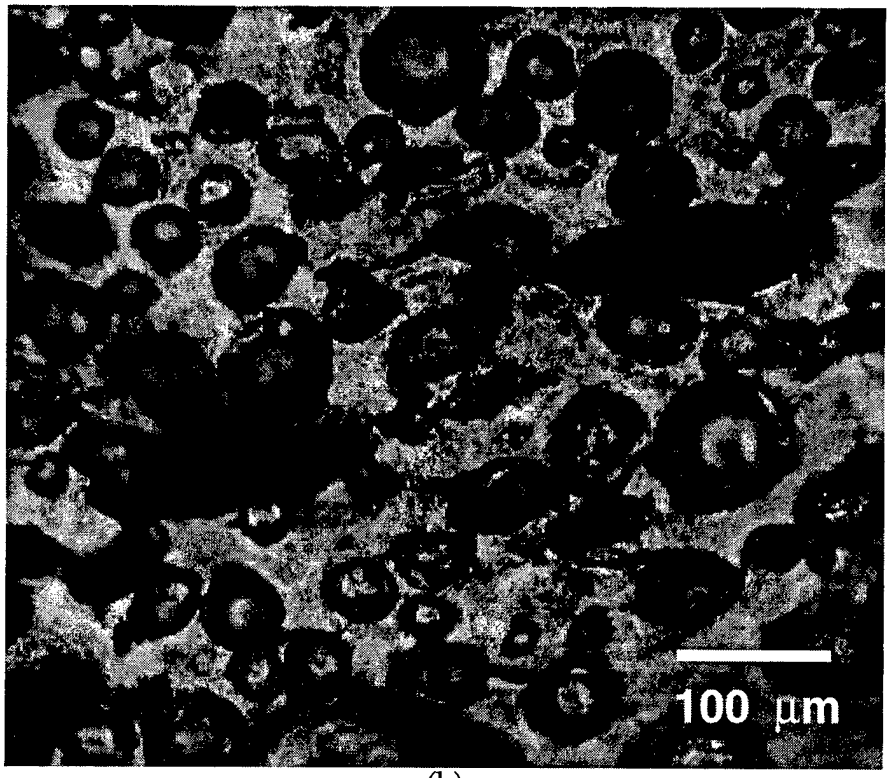

(b)

Figure 15 - Micrographs of porous polymer region with non-uniform microstructure in the unloaded (a), and compressed (b), states.

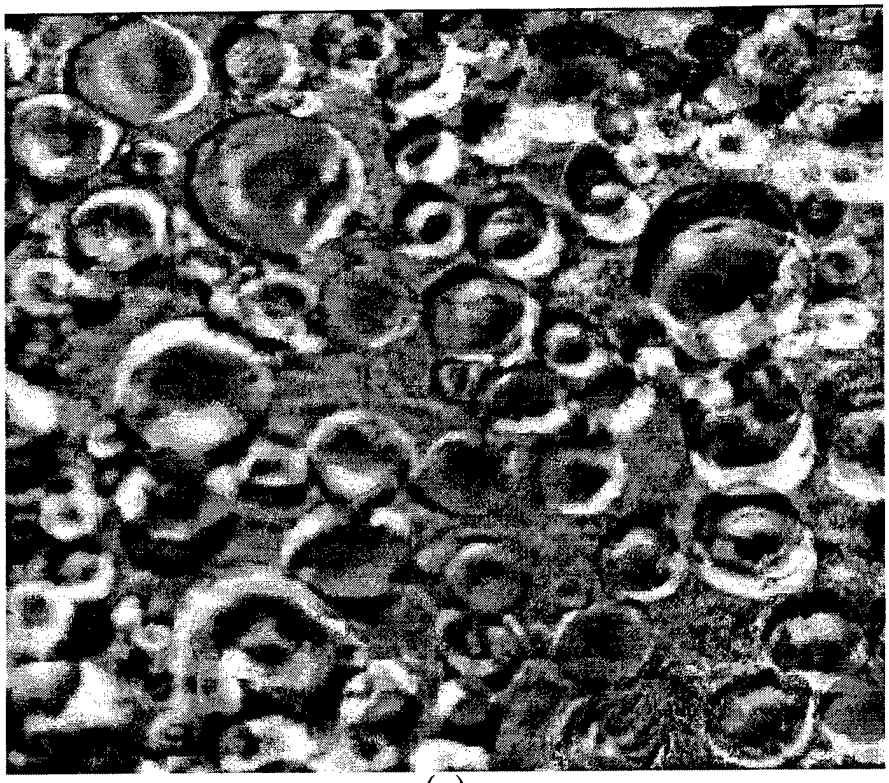

(a)

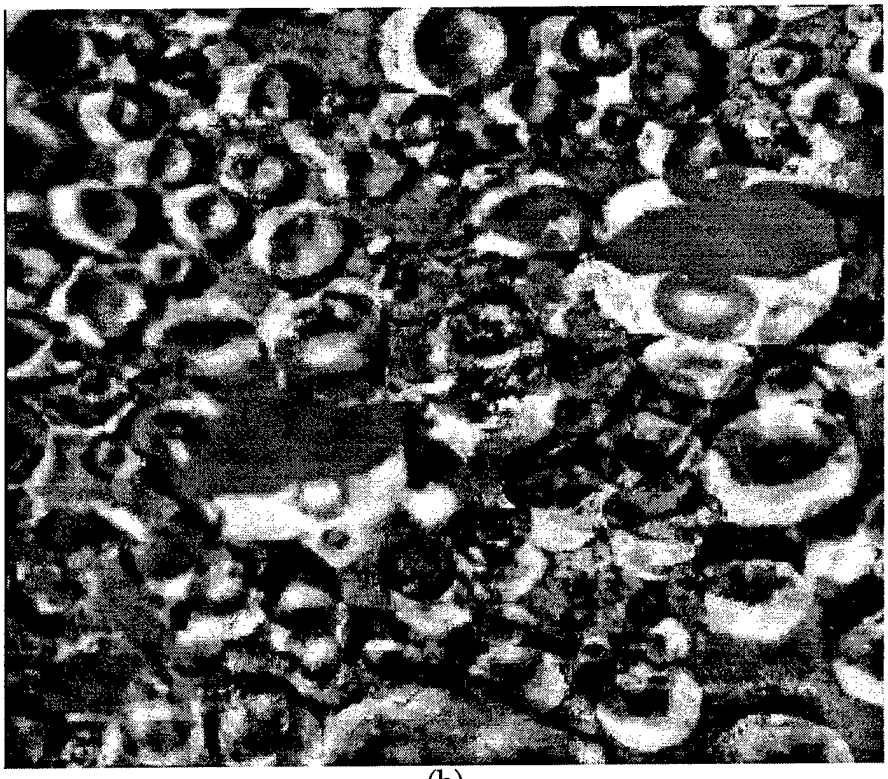

(b)

Figure 16 - Difference images of the uniform (a), and non-uniform (b), regions of the porous polymer microstructure.

3.0 FEM Modeling

Finite element modeling was conducted in order to better understand the effects of the non-homogeneous microstructure on the overall bulk mechanical behavior. This section will cover the model generation, the mechanical property input data and model, the imposed boundary constraints, model loading, and the results.

3.1 Model Generation

The finite element model used in this study was developed from an example of the actual material microstructure. Previous modeling studies on porous metals [9-13], incorporating the effects of complex microstructures, have convinced the authors that rendering a model as faithful to the microstructure as is possible is the only way to capture many of the nuances of the material response.

The microstructure chosen for modeling was presented previously in Fig 15a. The image of this microstructure under compression (Fig. 15b) can thus be compared to the model response. Digital image analysis was used to measure the area and centroid position of each feature in the field. A total of fifty nine features were incorporated into the final model. The feature areas were converted into circles of equivalent areas which were placed at the centroid positions. The circle radii were eroded, as necessary, to provide suitable, minimal ligament dimensions between pores, and with the boundary frame, to satisfy element size and shape requirements. Generally, the erosion was about 10% but went as high as 25% in a few cases. Figure 17 presents the final relative feature sizes and positions superimposed on the original microstructure. A good correlation exists between the actual and model features.

The circle position and radii data were read into the pre- and post-processor HyperMesh Version 2.0 [14]. HyperMesh was used to construct the 2D models that contained the 59 holes. The 2D automeshing features available in HyperMesh were used to create the Abaqus models. The finite element simulations were performed using ABAQUS/IMPLICIT 5.4 and utilized CPE8H and CPE6H elements. CPE8H elements are plane strain, 8 noded, biquadratic, hybrid, linear pressure elements. CPE6H elements are plane strain, 6 noded quadratic, hybrid, linear pressure elements. The finite element model contained 3001 elements with 9937 nodes. There were 2910 CPE8H elements and 91 CPE6H elements. The finite element mesh is shown in Figure 18.

The pores believed to be the Expancel microspheres were modeled both as perfect voids and as stiffened shells. The former is easier to implement while the latter is a better approximation to the actual problem. The effect of the harder plastic in the shell of the microsphere was introduced by stiffening the first row of elements around each pore, except for the two large central pores. These two are believed to be caused by entrapped gas (see Fig. 10) and thus contain no shell. Since the shell polymer was approximately one hundred times stiffer than the

matrix polymer but only had a shell thickness of 0.1 μm, the stiffness of the first row of elements around the pores was increased by only a factor of ten. This modified mesh is shown in Figure 19 with the stiffened elements highlighted. This approximation represents a compromise approach that accounted for the stiffness associated with the microsphere while eliminating the need to produce a region of very fine elements around the pores in order to model the shells. Including the fine elements may have produced a model with too many elements to analyze with existing resources.

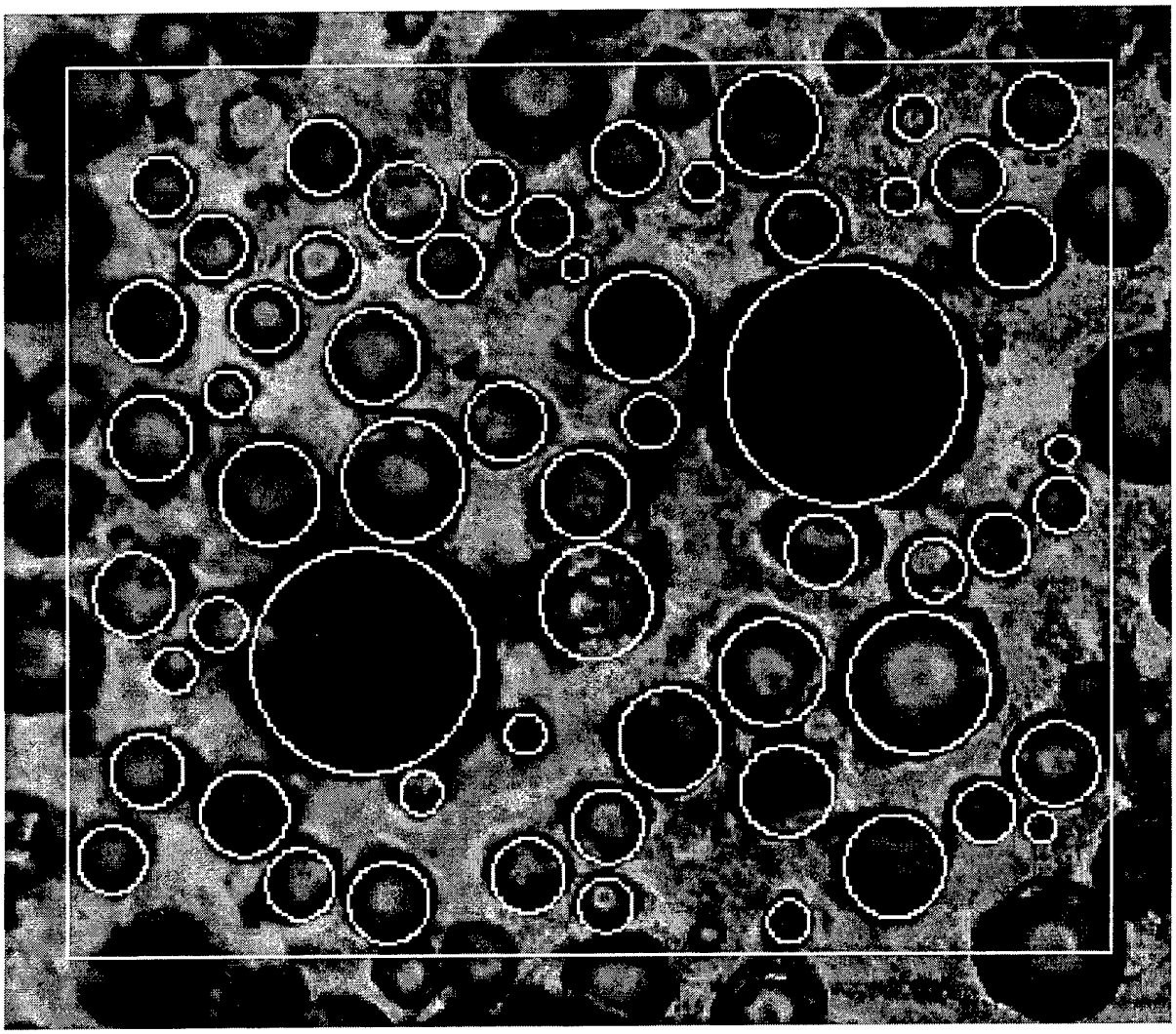

Figure 17 - Schematic diagram showing congruence of FEM model and the porous polymer microstructure.

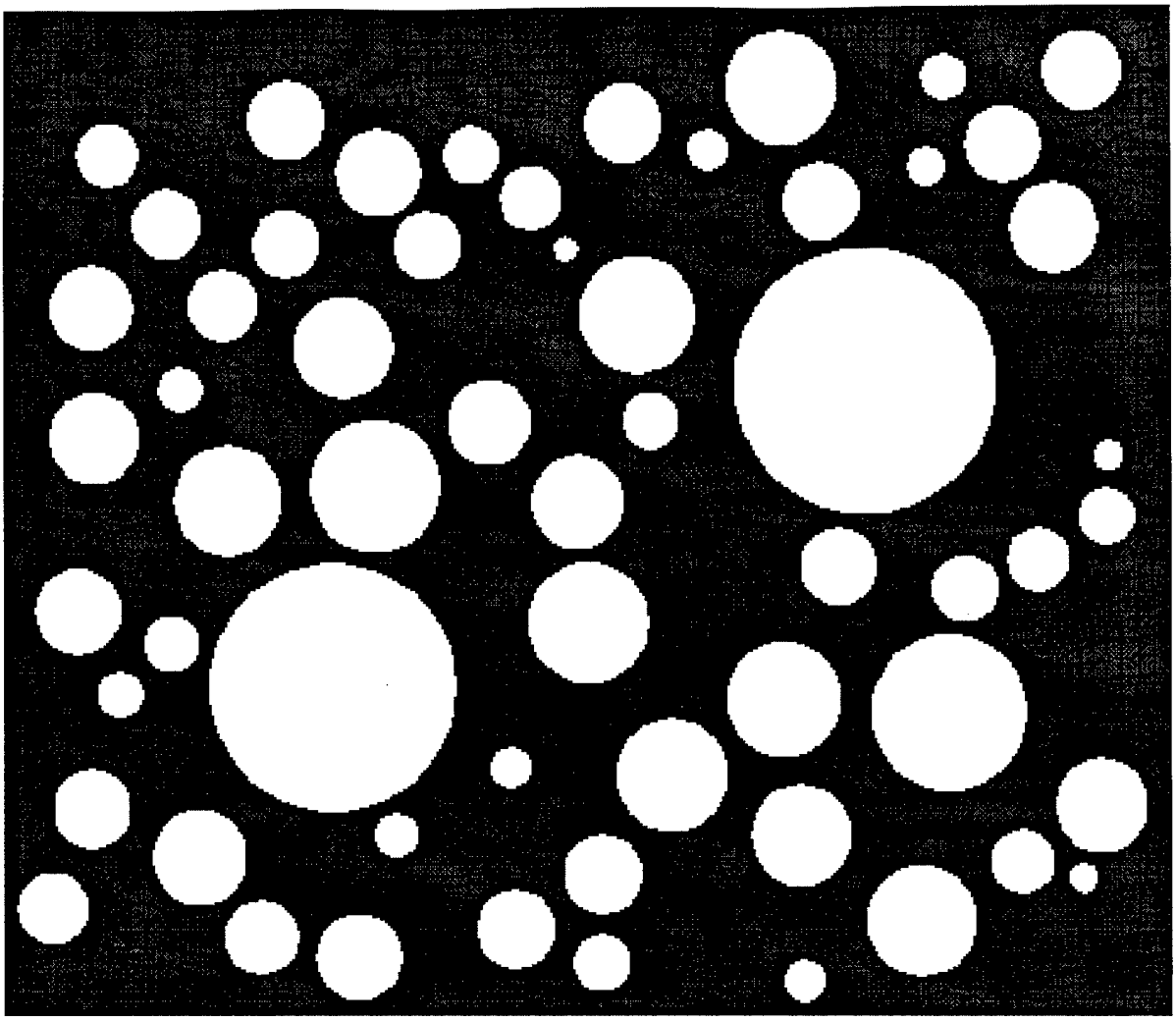

Figure 18 - Finite element mesh used to model pores as perfect voids.

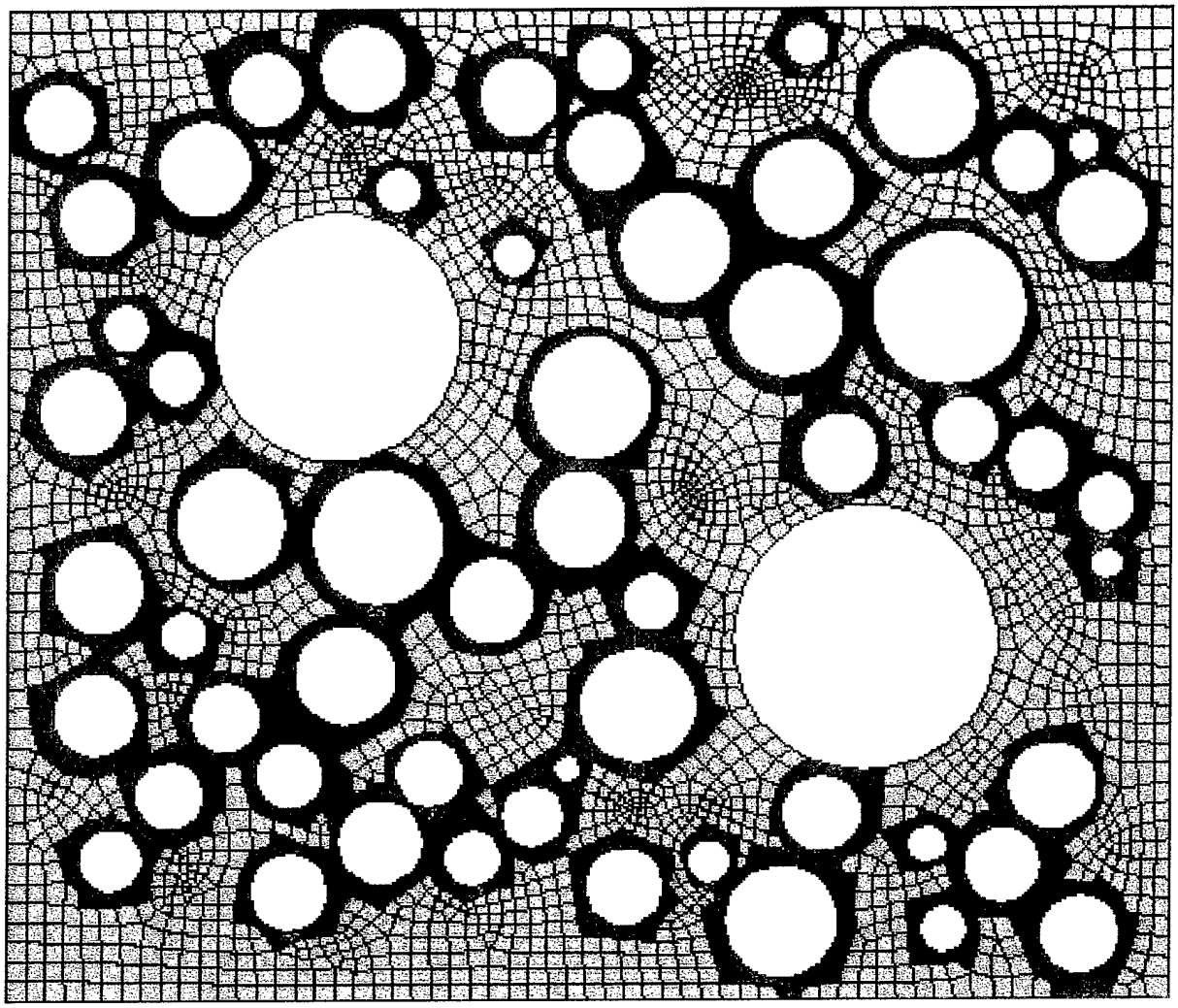

Figure 19 - Finite element mesh used to model pores as shells, with the shells highlighted.

3.2 Mechanical Property Input Data, Imposed Constraints, and Model Loading

A hyperelastic material model [15] was used for the matrix polymer. The nominal stress-nominal strain response of the neat polymer matrix material was obtained from the uniaxial compression and planar compression tests (Figs. 3 and 4) and used as inputs to the model. ABAQUS used these results to generate a material curve with the "*hyperelastic" option. Pores with shell reinforcements were run with an elastic material model utilizing the "*elastic" option.

The model was loaded by uniform boundary displacement derived from the experimental compression images. Linear multi-point constraints maintained the rectangular shape of the model during deformation. The top of the model was displaced downward. The sides were proscribed to displace outward at a rate of 20% of the vertical displacement. This value accounts for the constraint generated by adjacent material and was obtained from estimates of the Poisson strains measured on "no load" and "compressed" image pairs during scaling operations. The correlation between the applied compressions and measured displacements is shown in Figure 20. The lower edge of the model was constrained in the y-direction. The RIKS solution method was selected to apply these loads.

These finite element models were performed on a Cray YMP-EL computer. Postprocessing of the data files was done with Patran P3 Version 5.1 and HyperMesh 2.0. Contour plots were generated from the finite element results.

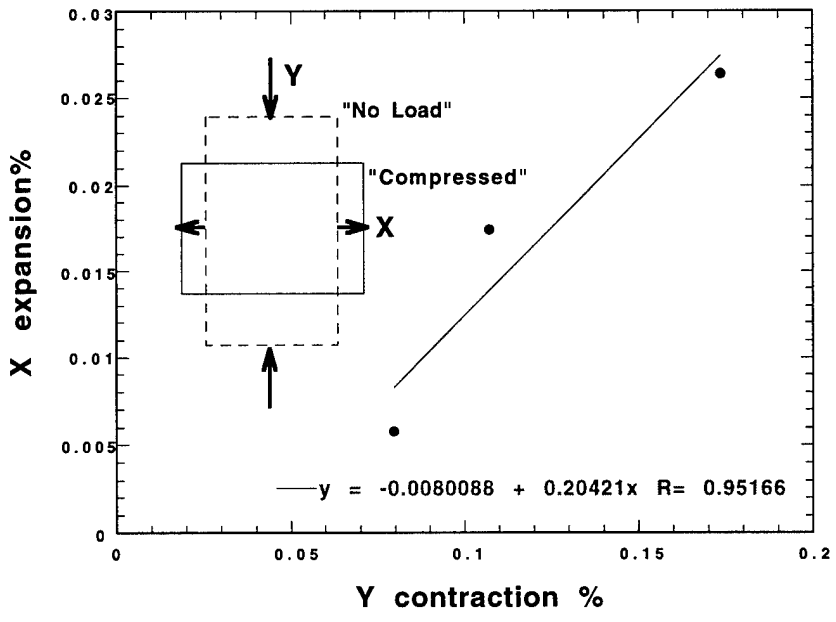

Figure 20 - Constraint boundary conditions derived from scaling factors measured when constructing difference images.

3.3 Results

The results of the finite element modeling indicate that correct modeling of the shell stiffening and the complex microstructure are both important. Figure 21 presents the ε_{yy} strain contours for the perfect void model at a total strain of 9.5%. Essentially all of the ε_{yy} strain values are between 0.120 and -0.120. Figure 22 presents the same information for the shell-stiffened model. However, for this case, the strain values range from 0.300 to -0.420.

The differences in strain localization are significant. Note that in the perfect void model the deformations are relatively homogeneous, with smaller pores as likely as larger ones to be distorted. Alternately, the shell stiffened model shows that the smaller pores are less distorted than the larger pores, and that a band of severely deformed material (running from the lower left to upper right of the figure) has localized between the larger pores. The shell stiffened results appear to mimic the actual deformed shapes better than the void model (see Fig. 15b). The Expancel microspheres are composed of a thermoplastic material and may be more likely to permanently deform in the localized region.

The inclusion of shell-polymer interface phenomena was considered to be beyond the scope of this prelimnary study. Future models could include this feature and examine the role of these mechanisms.

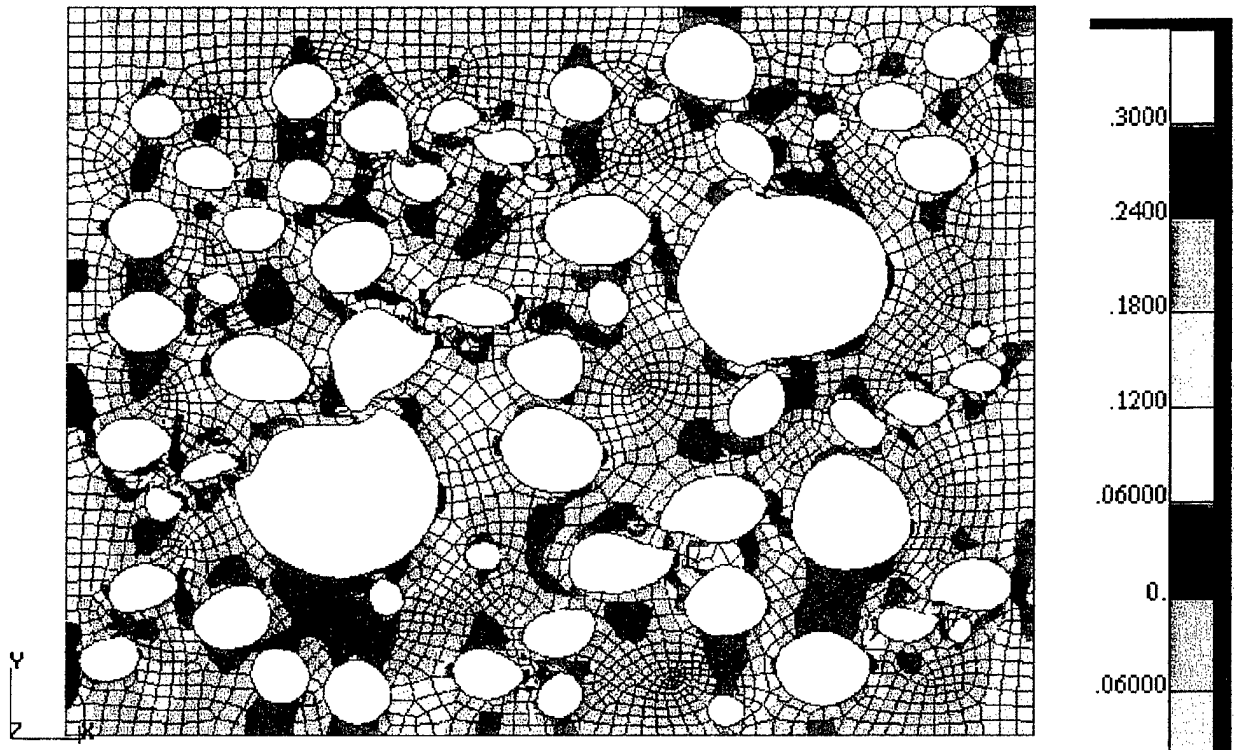

Figure 21 - The ε_{yy} strain contours for the perfect void model at a total strain of 9.5%. Scale is indicated at the right.

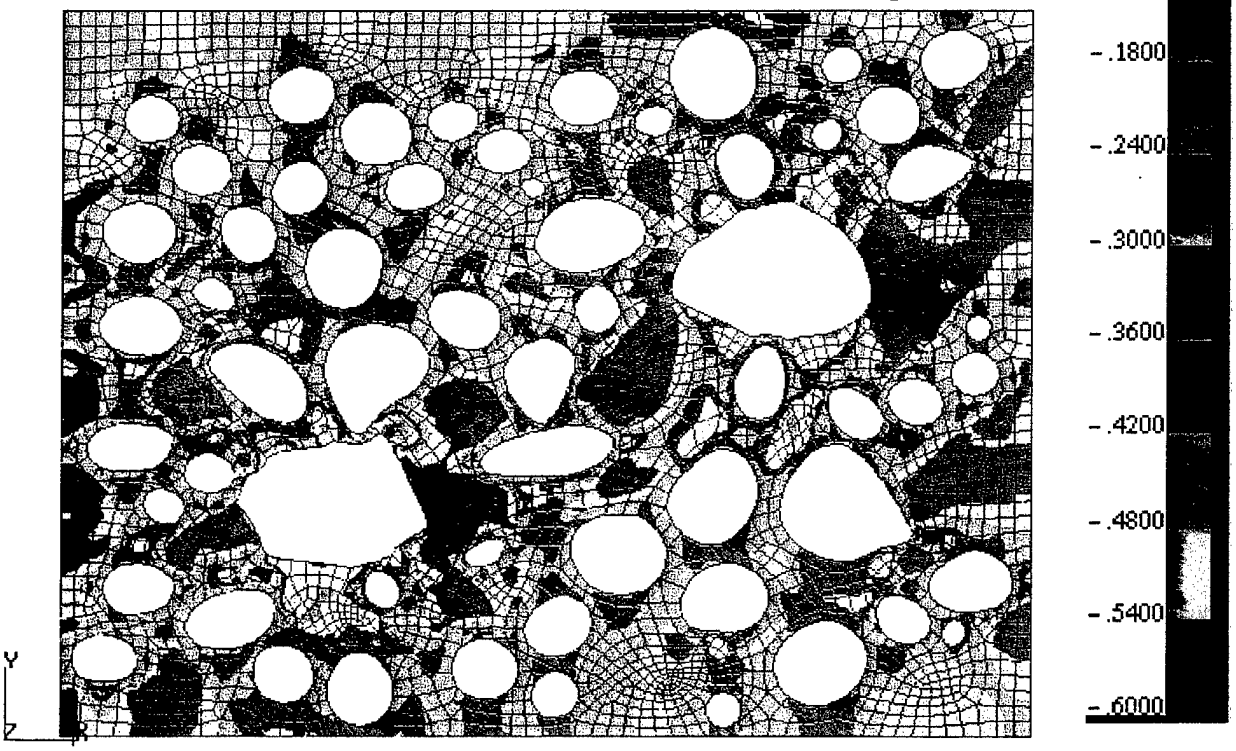

Figure 22 - The ε_{yy} strain contours for the shell-stiffened model at a total strain of 9.5%. Scale is indicated at the right.

4.0 Wave Propagation

Using the same material microstructure model as shown in Figure 17, numerical simulations of ultrasonic wave propagation were conducted. These simulations were carried out on NRL's CM-5 massively-parallel-processor (MPP) computer. They employed explicit finite-differencing, were completely parallel, and modeled sharp interfaces accurately. A similar technique was used in earlier work on visualization of ultrasonic pulses [16].

4.1 Model Inputs

The elastic constants and physical properties of the polymer without voids were used in the modeling. Lamé constants of $\lambda = 3.86 \times 10^{10}$ dynes/cm^2 and $\mu = 0.2 \times 10^{10}$ dynes/cm^2, and a density of 1.04 gm/cm^3 were utilized. The shear modulus is frequency dependent but a constant value equal to the value at 10 MHz was used. These constants imply a longitudinal wave velocity of 2.02 mm/μs and a shear wave velocity of 0.44 mm/μs. The slow shear wave velocity implies a small shear wavelength. The pores were modeled as perfect voids. Shell stiffening and any internal pressurization were ignored.

Plane compression waves (CW) with frequencies of 15 MHz and 7.5 MHz were imposed on the model. Ultrasonic frequencies were used to obtain a sufficient number of wavelengths over the computational grid. Grid sizes modeled were 2048 x 2048 cells with the grid spacing being 0.9 μm. The small cell size was selected in order to be able to model the smallest circular void with sixteen cells of the Cartesian grid spanning the diameter. A sponge or damping region 100 cells wide, with exponentially increasing damping, was used to eliminate reflected waves from the grid boundaries. "Snapshot" images, taken at three different timesteps during the propagation event, were made of the 1024 x 1024 cell region in the vicinity of the porous microstructure.

4.2 Results

The results for this model indicate strong multiple scattering due to the presence of the pores. The models ran very fast; grids of 1024 x 1024 cells could be updated one timestep every 10 milliseconds. A total of 2000 timesteps were computed. The snapshots shown in Figure 23 for the 15 MHz waves show that the waves penetrate only several void diameters into the porous region. The longitudinal wavefronts appear to be mode-converted (due to Rayleigh waves circumnavigating around the pores) into very slow shear waves (with wavelengths that are much shorter than the longitudinal waves) which linger near the pores. Similar results are obtained for the 7.5 MHz case, shown in Figure 24.

Much larger grids, with many more pores, would be needed to model the propagation of lower frequency waves using this technique. Furthermore, internal damping effects may be included in future work but were not considered here. Finite element techniques may be required to adequately model lower frequencies.

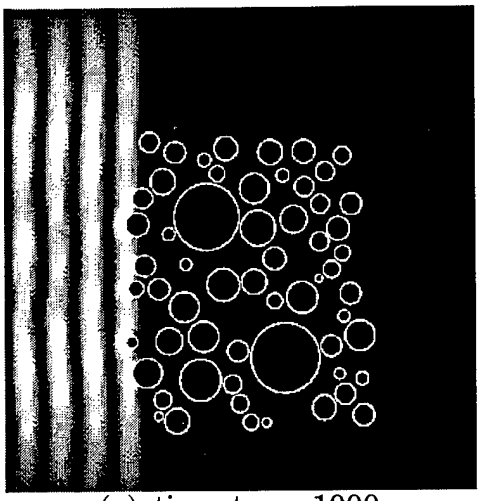

(a) timestep = 1000

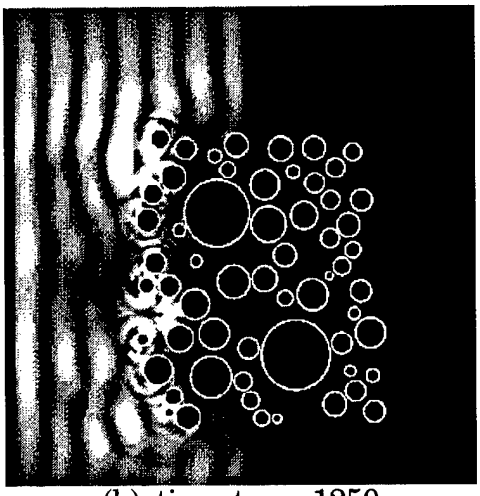

(b) timestep = 1250

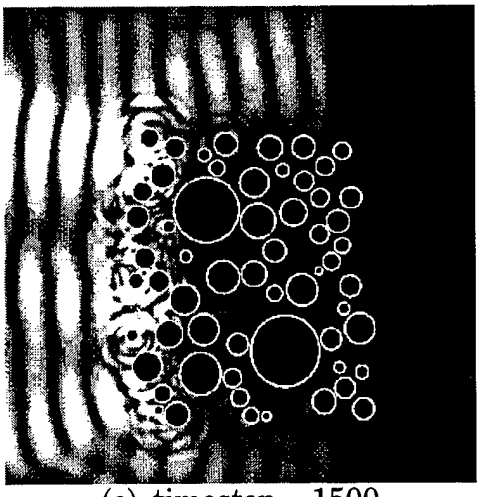

(c) timestep = 1500

Figure 23 - 15 MHz compression wave propagating through a porous polymer microstructure at three different timesteps.

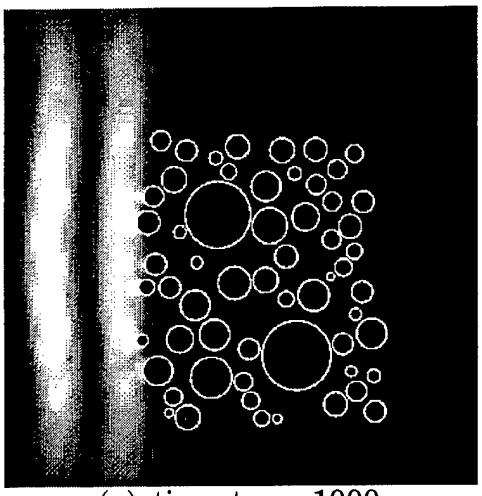

(a) timestep = 1000

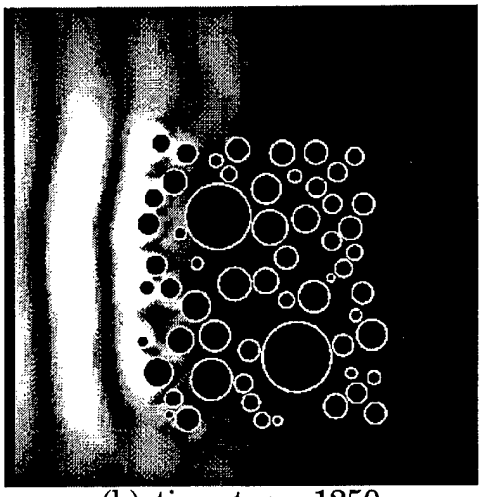

(b) timestep = 1250

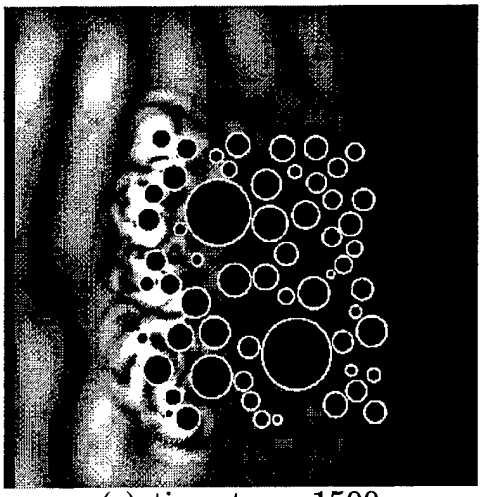

(c) timestep = 1500

Figure 24 - 7.5 MHz compression wave propagating through a porous polymer microstructure at three different times.

5.0 Nondestructive Evaluation (NDE)

Most polymers are electromagnetically low-loss materials. Consequently, measurement of the dielectric properties of these materials is an excellent choice for their nondestructive evaluation. Initial attempts to employ microwave dielectric measurements to detect variability in material properties for these polymeric materials were successful and are reported herein.

5.1 Microwave Dielectrometry

Microwave energy was chosen to characterize the neat and porous polymer materials. Energy transmitted into the material is consequently reflected back into a device for measurement. Two measurements, amplitude and phase, are recorded. The amplitude reading is basically a scalar quantity and represents the algebraic ratio of the reflected wave from the polymer material and the devices internal reference standard. This measurement also represents the resistive component which dissipates energy. The second measurement is the phase difference between the incident wave and the reflected wave from inside the material. This value relates to the reactive component of the material which does not dissipate energy. In general, these measurements will be a function of the microwave frequency.

The dielectric properties of a polymer mixture depend on several factors. These include: the dielectric properties of the constituents, the volume fractions of the constituents, the polymer cure state, and the physical and mechanical properties dependent on the cure state. One may consider the porous polymer to be a mixture of the neat polymer and the microspheres, and use two-phase spherical mixing models for the analysis of data. Therefore, predictions of porosity level or gas (air) volume fraction from frequency-dependent dielectric properties may be possible.

The device used for this initial investigation is called a microwave dielectrometer. The advantages of this device are: useful penetration into low-loss materials, high spatial resolution, non-contact and one-sided access measurement capabilities, and the availability of commercial instrumentation. The dielectrometer has an operational frequency of approximately 5.4 GHz, with an effective aperture of 10.69 mm and a wavelength 17.65 cm in air. The output power for this device is relatively small (i.e., less than 1 microwatt / cm^2 at 5.0 cm), thus making it a relatively safe instrument to operate without causing any damage to the material.

5.2 Measurements

Initial microwave dielectrometer measurements show a distinct difference between the neat material and the porous polymer. As shown in Figure 25, the dielectric constant measured for the neat material is approximately $\varepsilon_{host} = 4.29$, while $\varepsilon_{mix} = 3.13$ for porous polymer material, from the top region, containing the microspheres. Since the microspheres contain a gas, one would expect the dielectric constant for the material to shift toward the dielectric constant of air

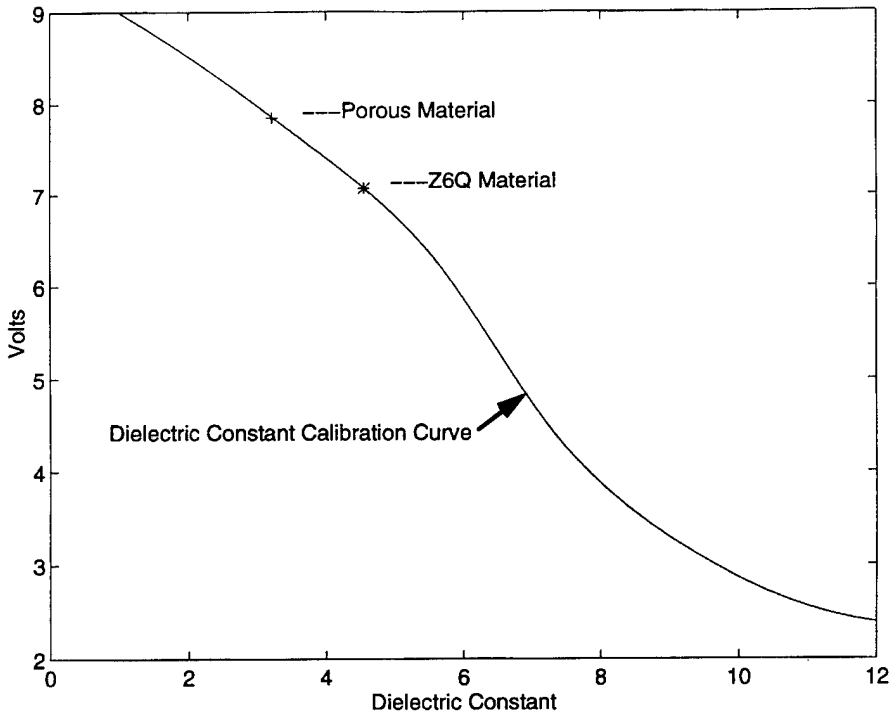

Figure 25 - 5.4 GHz microwave dielectric constant calibration curve and measurements on neat and porous polymer samples.

(ε_{air} = 1.0), as shown in Fig. 25. The degree of shift should be related to the volume fraction of the gas and a linear rule of mixtures was assumed. The dielectric constant of such a mixture, ε_{mix}, would be given by:

$$\varepsilon_{mix} = (1\text{-}V_{pores}\ )\ \varepsilon_{host} + V_{pores} \cdot \varepsilon_{air} \quad .$$

Substituting the measured and assumed dielectric values, the NDE-derived volume fraction of pores, $V_{pore,,}$ is equal to 0.54. This agrees reasonably well with the corresponding image-analysis-derived volume fraction of 0.51. If one were to consider the case of moisture absorption within the porous material, a dielectric constant shift in the direction of the dielectric constant for water (ε = 78) would be expected. Similarly, one could model this situation analytically, and compute the moisture content.

Dielectric data were taken from various sections of the porous material. Scatter in this data indicate that there are regions where the distribution of microspheres may not be uniform throughout the material. Such variations were also observed in data for the neat material. Computerized data acquisition and mapping of the spatial variation of the dielectric constant could provide "images" of the microsphere distribution.

6.0. Summary and Future Work

Porous polymers exhibit complex microstructures which affect their mechanical and physical properties. Pores in the microstructure are the result of the addition of polymer microspheres, and potentially by gas entrained during mixing operations. The entrained gas pores can form long strings and sheets which may act as defects in the structure. A combination of direct observation and finite element modeling has shown that accounting for the stiffening effect of the microspheres is important, and that strain localization occurs due to microstructural heterogeneity and interactions generated by the large gas pores. Permanent creep deformations can be imparted to the material in relatively short times, perhaps due to the localizations previously noted. Initial investigations into wave propagation and nondestructive evaluation by microwave dielectrometry were successful.

In general, more work needs to be performed to relate permanent changes in the microstructure to dynamic material property changes. Specific recommendations for future work include:

- Complete characterization of pores in neat polymer,
- Further characterization of gas pore clustering,
- Creep response of the neat polymer,
- Creep response of the porous polymer,
- Microstructural characterization of creep-deformed materials,
- Inclusion of polymer matrix - shell coupling effects,
- Two- and three-dimensional finite element model analysis,
- Finite element modeling of wave propagation,
- Investigation of microwave dielectrometry for NDE,
- NDE to assess fabrication quality and track service life.

Completion of these tasks might allow for the optimization of the material microstructure to the needs of designers of actual structures.

ACKNOWLEDGEMENTS

This work was supported by the Office of Naval Research under a grant from Dr. Roshdy Barsoum and by the Naval Research Laboratory's basic research program. The authors are grateful to NSWC-Caderock for providing material samples and data.

REFERENCES

1. W. H. El-Ratal and P. K. Mallick, "Elastic Response of Flexible Polyurethane Foams in Uniaxial Tension," Trans. of the ASME, *J. of Eng. Mat. and Tech.*, **118** (April 1996), pp. 157--161.

2. G. Ben-Dor, G. Cederbaum, G. Mazor, and O. Igra, "Well-tailored compressive stress-strain relations for elastomeric foams in uniaxial stress compression," *J. Mat. Sci.*, **31**(1996), pp. 1107-1113.

3. J. D. Rehkopf, G. M. McNeice, and G. W. Brodland, "Fluid and Matrix Components of Polyurethane Foam Behavior Under Cyclic Compression," Trans. of the ASME, *J. of Eng. Mat. and Tech.*, **118** (Jan. 1996), pp. 58--62.

4. private communication, Dr. Roshdy Barsoum, Office of Naval Research.

5. Dr. J. D'Lubac, NSWC-Caderock.

6. At the time of this report, Expancel Inc. was located at 2150 H Northmont Parkway, Duluth, GA 30136. Telephone Number: (770)-813-9126, Fax: (770)-813-8639.

7. E. E. Underwood, *Quantitative Stereology*, Addison-Wesley Publishing Co., 1970.

8. R. K. Everett and J. H. Chu, *J. Comp. Mat.*, **27**, No. 11, pp. 1128-1144.

9. P. Matic, A. B. Geltmacher, D. P. Harvey, R. J. Bonenberger, and A. Kee, "Model Experiments and Finite Element Analysis for Insight into Three Dimensional Ductile Fracture and Porous Material Response," 1995 ABAQUS User's Conference, Paris, France. pp. 579-593.

10. A. B. Geltmacher, P. Matic, and D. P. Harvey, "An Experimental Study Evaluating Macroscopic Cavity Interactions as a Model of Microvoid Ductility," submitted to *ASME Jotnal of Engineering Materials and Technology*.

11. A. Kee, P. Matic, and J. M. Wolla, "A Computational Study of Elongated Pore Interactions in a Low Density Porous Copper," submitted to *Materials Science and Engineering*.

12. A. Kee, P. Matic, and L. Popels, "A Two Dimensional Computional Study of a GASAR Porous Copper Microstructure," submitted to *Materials Science and Engineering*.

13. S. Moorthy and S. Ghosh, "A Model for Analysis of Arbitrary Composite and Porous Microstructures With Voronoi Cell Finite Elements," to be published in *Int. J. Numerical Methods in Engineering*, 1996.

14. HyperMesh is a product of Altair Computing, Inc., Troy, MI.

15. ABAQUS/Implict User Manual Version 5.4, Hibbitt, Karlson, and Sorenson, Inc., Pawtucket, RI, 1994.

16. R. S. Schecter, H. H. Chaskelis, R. B. Mignogna, and P. P. Delsanto, "Real-Time Parallel Computation and Visualization of Ultrasonic Pulses in Solids," *Science*, **265** (26 Aug., 1994), pp. 1188-1192.